Reliable Phase Selection Method for Transmission Systems Based on Relative Angles Between Sequence Voltages

Abdallah A. Aboelnaga and Maher A. Azzouz, *Senior Member*, *IEEE*

***Abstract*—Fault currents emanating from inverter-based resources (IBRs) are controlled to follow specific references to support the power grid during faults. However, these fault currents differ from the typical fault currents fed by synchronous generators, resulting in an improper operation of conventional phase selection methods (PSMs). In this paper, the relative angles between sequence voltages measured at the relay location are determined analytically in two stages: ① a short-circuit analysis is performed at the fault location to determine the relative angles between sequence voltages; and ② an analysis of the impact of transmission line on the phase difference between the sequence voltages of relay and fault is conducted for different IBR controllers. Consequently, new PSM zones based on relative angles between sequence voltages are devised to facilitate accurate PSM regardless of the fault currents, resistances, or locations of IBR. Comprehensive time-domain simulations confirm the accuracy of the proposed PSM with different fault locations, resistances, types, and currents.**

***Index Terms*—Fault resilience, fault type identification, phase selection method, inverter-based resources, control function, renewable energy source, sequence voltage.**

I. Introduction

THE penetration of renewable energy sources (RESs) is increasing in both transmission and distribution networks due to their merits in reducing fuel consumption and greenhouse gas emission [1]. However, RESs are mainly integrated into the power grid as inverter-based resources (IBRs), whose generated current possesses characteristics that differ from synchronous generator (SG) fault currents [2]. Thus, the penetration of RESs introduces challenges to the power grid regarding stability and protection. Since legacy protection systems, e.g., distance relays, direction relays, and phase selection methods (PSMs), are designed based on SG fault characteristics, they may operate improperly when faults are fed from RESs [3], [4].

Phase selection is an essential protection function that determines the faulty phase(s). PSM is considered as an imperative protection function in transmission systems as it is a prerequisite function for distance, single-pole tripping, and fault location [5]. Conventional PSMs can be classified according to the type of the processed electrical quantities into two categories: ① PSMs for transient quantities, which are based on high-frequency components, traveling wave, or wavelet transform [6] - [8], and ② PSMs for steady-state quantities, which are based on comparing the magnitudes and/or phases of electrical quantities [9], [10]. It is worth mentioning that most conventional relays depend on steady-state quantities as they do not require expensive and accurate data analysis [11], [12]. Despite the reliability of conventional PSMs in legacy power grids, they might perform incorrectly when fault currents emerge from IBRs [13]. Accordingly, many researchers have recently endeavored to solve the protection problems in the presence of IBRs.

Some researchers pursue solving the phase selection problem by controlling the IBR to inject adequate fault current. In [13], the negative-sequence (NS) current is controlled to enforce the inverter NS model to be equivalent to an impedance with an X/R ratio equal to the ratio of traditional network. In [14], the NS current angle is controlled based on either the measured zero-sequence (ZS) current angle or the positive-sequence (PS) current angle to guarantee proper current-angle-based PSM, while both the NS and ZS current angles are controlled in [15]. These methods enhance the PSM operation; however, the reactive current generation requirements are not taken into consideration, which limits their applicability. In [16], the NS and PS currents are controlled to guarantee the correct operation of PSM as well as applying reactive current requirements imposed by grid codes (GCs), but it impairs the sensitivity of the relay operation. In addition, there is no guarantee that the aforementioned methods operate properly in different microgrid topologies. It is worth mentioning that [14]-[17] require determining the fault type at the IBR terminal accurately as a prerequisite for controlling the IBR current to mimic SG fault current characteristics. Thus, it is crucial to develop an accurate PSM that

Manuscript received: August 31, 2023; revised: January 10, 2024; accepted: April 28, 2024. Date of CrossCheck: April 28, 2024. Date of online publication: May 23, 2024.

This work was supported by the Natural Sciences and Engineering Research Council of Canada (NSERC) (No. RGPIN-2023-0368) and Qatar University (No. QUCG-CENG-24/25-485). The findings achieved herein are solely the responsibility of the authors.

This article is distributed under the terms of the Creative Commons Attribution 4.0 International License (http://creativecommons.org/licenses/by/4.0/).

A. A. Aboelnaga is with the Department of Electrical and Computer Engineering, University of Windsor, Windsor, ON N9B 3P4, Canada, and he is also with Electrical Power and Machines Department, Faculty of Engineering, Ain Shams University, Cairo 11566, Egypt (e-mail: aboelna@uwindsor.ca).

M. A. Azzouz is with the Electrical Engineering Department, Qatar University, Doha, Qatar (e-mail: mazzouz@qu.edu.qa).

DOI: 10.35833/MPCE.2023.000616

can determine the fault type precisely at the IBR terminal to enable the IBR controller to operate strictly.

On the other hand, other researchers attempt to modify conventional PSMs to enhance their security and dependability during faults that emerge from IBRs. Reference [17] attempts to enhance the current-angle-based PSM by allowing the relay to operate only during a certain period of time after the fault inception, but some of the results still show maloperation [17]. In [18], the faulty phase is determined by comparing the NS and ZS voltage angles and the NS and PS voltage angles. Reference [19] compares the sequence voltage angles for ground faults while comparing the voltage phase angles in ungrounded faults. These methods show proper operations; however, they ignore the arc resistance effect in the analyses. Thus, these methods are susceptible to failure with large arc resistances. Reference [20] attempts to combine the faulty phases determined from both the voltage-angle-based and an improved current-angle-based PSM. However, this combination can aggravate the problem, as a failure in any method could lead to the incorrect identification of faulty phases. In [21], the faulty phase is pinpointed based on the superimposed voltage calculated at the fault location by computing the pre-fault impedance and augmenting it in the current-angle-based classifier equations. In [22], the faulty phase is determined based on current-angle-based PSM by improving the PSM zones by adding an online compensation angle. However, these calculations could increase the computational time for faulty phase identification. In [23], the faulty phase is identified by utilizing a new method of computing the relative angle between sequence fault currents. These methods assume that transmission lines (TLs) have a negligible effect on the PSM accuracy. While these methods function properly in microgrids and distribution systems, they may encounter failures in transmission systems. According to the authors' knowledge, there is no method elaborating on the effect of TLs on the relative sequence voltage angles between the relay and fault locations for lines connected with IBRs. Thus, it is necessary to investigate the impact of TL at various IBR controllers on the PSM accuracy, and determine an effective PSM that can operate properly in power grids containing IBRs. The contributions of this paper are described as follows.

1) The practical range for relative angles is elucidated between sequence voltages calculated at the fault location.

2) The impacts of TL impedance and IBR controllers on the relative angles are interpreted between similar sequence voltages measured at the fault and relay locations through analytical methods.

3) A comprehensive PSM is proposed based on comparing sequence angles between NS and ZS voltages and between NS and PS voltages to ensure the precise and secure phase selection for different IBR controllers, fault resistances, and fault locations.

II. Analysis of Relative Angles Between Sequence Voltages

In this section, short-circuit analyses are performed on a sample power system shown in Fig. 1, for single-line-to-ground (SLG), line-to-line-to-ground (LLG), and line-to-line (LL) faults, to determine the relative angle between the NS and ZS voltages measured at the fault location, i.e., $\delta_F^0 = \angle V_F^- - \angle V_F^0$, and that between the NS and PS voltages, i.e., $\delta_F^+ = \angle V_F^- - \angle V_F^+$. In Fig. 1, V_{IBR} is the voltage at the IBR terminal; Z_{Tr} is the transformer impedance; V_{R12} and V_{R21} are the voltages measured by relays R_{12} and R_{21}, respectively; i_{R12} and i_{R21} are the currents measured by relays R_{12} and R_{21}, respectively; Z_L is the line impedance; and Z_{grid} is the grid equivalent impedance. It is noted that in this paper, NS, ZS, and PS are represented by superscripts –, 0, and +, respectively.

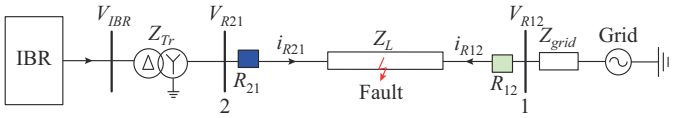

Fig. 1. Structure of sample power system.

A. SLG Fault Analysis

In this subsection, the sequence network for an a-phase-to-ground (AG) fault is analyzed, as a representative for SLG faults, to determine the relation between the sequence fault voltages, i.e., V_F^+, V_F^-, and V_F^0, and their relative angles. As shown in Fig. 2, the sequence fault currents, i.e., I_F^+, I_F^-, and I_F^0, are equal; thus, they are renamed in this subsection as I_F for simplification, while the sequence fault voltages are formulated by:

$$\begin{cases} V_F^- = -I_F Z_{th}^- \\ V_F^0 = -I_F Z_{th}^0 \\ V_F^+ = I_F\left(Z_{th}^- + Z_{th}^0 + 3R_g\right) \end{cases} \tag{1}$$

where Z_{th}^-, Z_{th}^0, and Z_{th}^+ are the NS, ZS, and PS Thevenin impedances at the fault location, respectively; and R_g is the ground fault resistance.

From (1), the relation between V_F^- and V_F^0 and that between V_F^- and V_F^+ are given by:

$$\begin{cases} \dfrac{V_F^-}{V_F^0} = \dfrac{Z_{th}^-}{Z_{th}^0} \\ \dfrac{V_F^-}{V_F^+} = \dfrac{-Z_{th}^-}{Z_{th}^- + Z_{th}^0 + 3R_g} \end{cases} \tag{2}$$

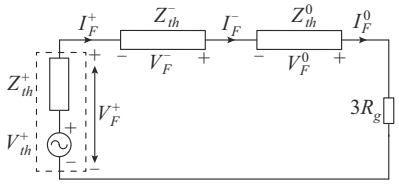

Fig. 2. Sequence circuit at fault location for an AG fault.

Hence, δ_F^0 and δ_F^+ are given by:

$$\begin{cases} \delta_F^0 = \angle Z_{th}^- - \angle Z_{th}^0 \\ \delta_F^+ = \angle Z_{th}^- - \angle\left(Z_{th}^- + Z_{th}^0 + 3R_g\right) - 180° \end{cases} \tag{3}$$

It is worth mentioning that in a typical transmission system, the PS, NS, and ZS equivalent impedance angles are almost equal, and they are around 80° [24]. Since the magni-

tude of the IBR equivalent impedance is much larger than the grid-side impedance, the Thevenin impedance is roughly equal to the grid-side impedance [25], i. e., $\angle Z_{th}^{+} \approx \angle Z_{th}^{-} \approx \angle Z_{th}^{0} \approx 80°$. Hence, it can be deduced that $\delta_F^0 \approx 0$, while δ_F^+ varies according to the magnitude of R_g, as shown in Fig. 3.

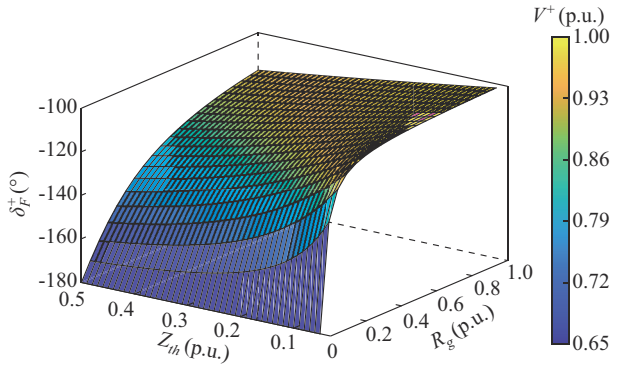

Fig. 3. δ_F^+ range for an AG fault.

It can be observed from Fig. 3 that $\delta_F^+ = -180°$ for solid faults, and it increases as R_g increases. It is also deduced that the effect of R_g on δ_F^+ increases while the magnitude of the Thevenin impedance, i.e., $|Z_{th}|$, decreases. Thus, to determine the maximum variation of δ_F^+ from the solid fault condition, the minimum value of $|Z_{th}|$ is utilized. Since the fault current in three-phase faults can reach 4 to 20 times its rated value [25], [26], the minimum value of $|Z_{th}^+| \approx 0.05$ p.u.. Besides, $|Z_{th}^-|$ is almost equivalent to $|Z_{th}^+|$ [27]; thus, the minimum value of $|Z_{th}^-| \approx 0.05$ p. u.. Meanwhile, $|Z_{th}^0|$ is usually higher than $|Z_{th}^+|$, i. e., $|Z_{th}^0| = k^0 |Z_{th}^+|$, where k^0 is a constant that depends on the neutral conductor size and varies from 1 to 5 [27]. In order to get the minimum value of $|Z_{th}^0|$, k^0 is selected to be 1, and the minimum value of $|Z_{th}|$ in Fig. 3 is selected, such that $|Z_{th}^+| = |Z_{th}^-| = |Z_{th}^0| = |Z_{th}| = 0.05$ p. u.. It can be observed from Fig. 3 that δ_F^+ varies from −180° for solid faults to −100° for high-resistive faults. However, the increase of fault resistance can reduce the PS voltage drop. The practical range for δ_F^+ for AG faults is limited to be $V_F^+ = 0.9$ p.u., and thus, δ_F^+ ranges from −180° to −110°.

B. LLG Fault Analysis

As a representative of LLG faults, the sequence network for a b-phase-to-c-phase-to-ground (BCG) fault is analyzed, as shown in Fig. 4. Accordingly, V_F^-/V_F^0 and V_F^-/V_F^+ are determined by (4), as demonstrated in Appendix A.

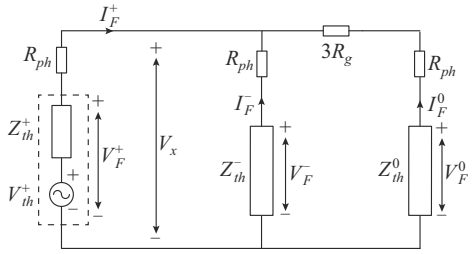

Fig. 4. Sequence circuit at fault location for a BCG fault.

$$\begin{cases} \dfrac{V_F^-}{V_F^0} = \dfrac{Z_{th}^-}{Z_{th}^0} \dfrac{Z_{th}^0 + R_{ph} + 3R_g}{Z_{th}^- + R_{ph}} \\ \dfrac{V_F^-}{V_F^+} = \dfrac{Z_{th}^-}{Z_{th}^- + 2R_{ph} + \dfrac{R_{ph}\left(R_{ph} + Z_{th}^-\right)}{Z_{th}^0 + R_{ph} + 3R_g}} \end{cases} \tag{4}$$

where R_{ph} is the arc resistance between faulted phases. Hence, for solid faults, δ_F^0 and δ_F^+ are given by:

$$\begin{cases} \delta_F^0 = 0 \\ \delta_F^+ = \angle \dfrac{Z_{th}^-}{Z_{th}^- + \dfrac{Z_{th}^-}{Z_{th}^0}} \approx 0 \end{cases} \tag{5}$$

However, to determine the values of δ_F^0 and δ_F^+ at different values of R_{ph} and R_g, Fig. 5 is determined by varying R_{ph} and R_g, while $|Z_{th}^-|$ and $|Z_{th}^0|$ are selected at their minimum values, i.e., 0.05 p.u., to get the maximum ranges for both δ_F^0 and δ_F^+. It can be deduced from Fig. 5(a) that R_{ph} has a neglectable effect on δ_F^0, while increasing R_g directly affects the value of δ_F^0. With large value of R_g, $\delta_F^0 \approx -\angle Z_{th}^0$; thus, δ_F^0 can vary from 0° to −80° in a BCG fault. However, the practical range of δ_F^0 is from 0° to −73°, as illustrated in Fig. 5(a). On the other hand, δ_F^+ is negligibly affected by R_g, but is substantially impacted by the value of R_{ph}, as shown in Fig. 5(b). For considerable R_{ph}, $\delta_F^+ \approx \angle Z_{th}^-$; hence, δ_F^+ can vary in a BCG fault from 0° to 80°. This range matches the total range determined in Fig. 5(b). However, the effective range of δ_F^+ is from 0° to 68°.

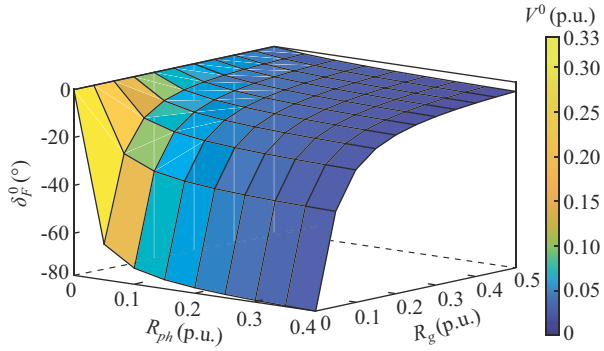

(a)

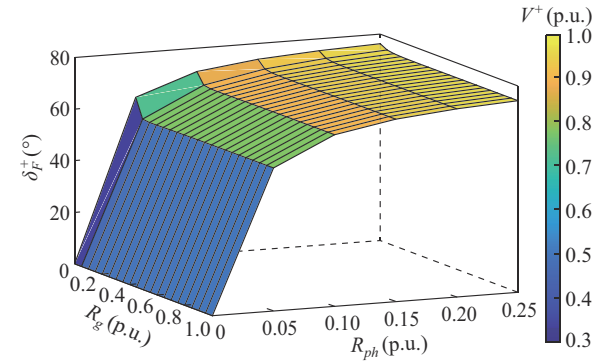

(b)

Fig. 5. Relative sequence angles for a BCG fault. (a) δ_F^0. (b) δ_F^+.

C. LL Fault Analysis

In this subsection, the sequence network for a b-phase-to-c-phase (BC) fault is analyzed. The relation between V_F^+ and V_F^- is derived from Fig. 6 as:

$$V_F^+ = V_F^- + I_F^+ R_{ph} = V_F^- \frac{Z_{th}^- + R_{ph}}{Z_{th}^-} \tag{6}$$

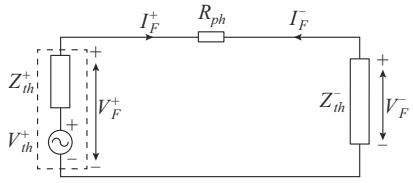

Fig. 6. Sequence circuit at fault location for a BC fault.

Thereafter, the ratio between V_F^- and V_F^+ is determined by:

$$\frac{V_F^-}{V_F^+} = \frac{Z_{th}^-}{Z_{th}^- + R_{ph}} \tag{7}$$

Consequently, it can be inferred that δ_F^+ is susceptible to R_{ph}. If $R_{ph}=0$, $\delta_F^+=0$. On the other hand, if R_{ph} is noticeable, $\delta_F^+ \approx \angle Z_{th}^- \approx 80°$. Figure 7 depicts the range of δ_F^+ for a BC fault against the wide ranges of $|Z_{th}^-|$ and R_{ph}. It is manifested that the theoretical range of δ_F^+ can vary from 0° to 80° for a BC fault, whereas the practical range is between 0° to 68°.

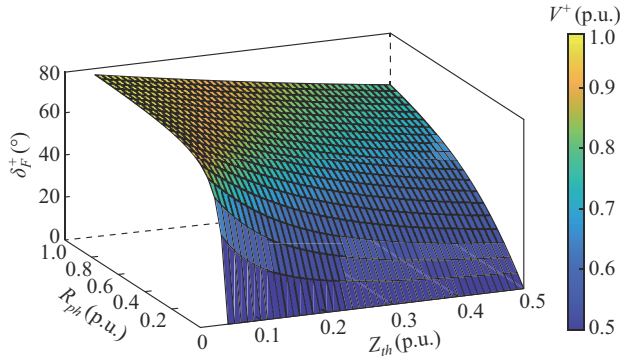

Fig. 7. δ_F^+ range for a BC fault.

III. Analysis of Phase Shifts Between Sequence Voltages

The TL introduces a voltage phase shift between sequence voltages measured at the relay and fault locations. This phase shift is negligible in conventional power grids; however, its impact is notable in the case of IBRs because their current angles differ from those of traditional sources. Hence, the impact of TLs should be analyzed to determine the phase angle between the NS and ZS voltages measured at the relay location, i.e., $\delta_R^0 = \angle V_R^- - \angle V_R^0$, and that between NS and PS voltages, i.e., $\delta_R^+ = \angle V_R^- - \angle V_R^+$.

A. ZS Voltage

The IBR is usually integrated into the power grid through an interfacing transformer, e.g., a delta/star-ground transformer. This transformer connection prevents any ZS current injection from the IBRs from flowing to the fault. Thus, the only source of ZS current that flows through the relay to the fault is from the ground path in the transformer. The equivalent single-line diagram (SLD) of the ZS circuit is illustrated in Fig. 8, where V_G^0 is the ZS voltage measured at the grid side; I_R^0 is the ZS current measured at the relay; I_G^0 is the ZS current supplied from the grid side; and Z_G^0 is the ZS equivalent impedance between the fault and the grid ground.

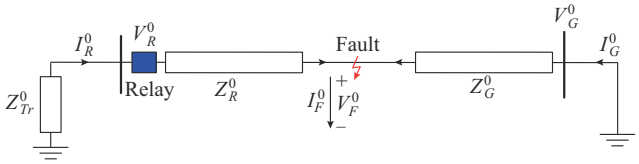

Fig. 8. Equivalent SLD of ZS circuit.

By analyzing Fig. 8, the ZS voltage measured at the relay side V_R^0 can be determined by:

$$V_R^0 = V_F^0 \frac{Z_{Tr}^0}{Z_R^0 + Z_{Tr}^0} \tag{8}$$

where Z_{Tr}^0 is the equivalent ZS impedance of transformer; and Z_R^0 is the equivalent ZS impedance between the relay and the fault location. Since $\angle Z_{Tr}^0 \approx \angle Z_R^0$, the relative angle between the ZS voltage measured at the relay and fault location, i.e., $\Delta\theta_{RF}^0 = \angle V_R^0 - \angle V_F^0$, is approximately equal to zero. This angle can be theoretically neglected, but its effect is considered as a margin when setting the proposed PSM zones.

B. NS and PS Voltages

In this subsection, the range of the phase shift between the NS voltages of relay and fault, i.e., $\Delta\theta_{RF}^- = \angle V_R^- - \angle V_F^-$, and that between the PS voltages of relay and fault, i.e., $\Delta\theta_{RF}^+ = \angle V_R^+ - \angle V_F^+$, are analyzed for different IBR controllers.

1) Conventional Controller

The controller is designed to inject only PS current, where a proportional-integral controller is used to track the reference current, and a feed-forward voltage is utilized to enhance the dynamic response of the controller. However, it diminishes the NS current similar to the balanced-current control strategy, i.e., $|I_{IBR}^-| \approx 0$. Hence, the effect of $\Delta\theta_{RF}^-$ is abandoned in both balanced and conventional controllers.

On the other hand, the full range of the PS voltage phase shift between the fault and relay location is required to be analyzed. To determine the maximum angle of $\Delta\theta_{RF}^+$, the system is studied at the furthest point from the fault, which is the IBR location, because increasing the impedance between the relay and fault location increases the phase shift. Figure 9 represents an equivalent SLD of the PS circuit of Fig. 1, where Z_R^+ is the maximum PS equivalent impedance between the relay (IBR) and fault location, while the IBR is represented by a current source of magnitude $|I_{IBR}^+|$ and phase $\theta_{VR}^+ - \phi^+$. The angle θ_{VR}^+ is the PS voltage angle measured at the IBR terminal, i.e., the relay location of the maximum phase shift; and ϕ^+ is the phase shift between the PS voltage and current of IBR.

Using Fig. 9, the relation between the voltage at the IBR, i.e., the farthest relay location, and fault location can be determined by:

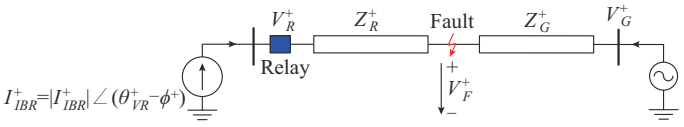

Fig. 9. Equivalent SLD of PS circuit.

$$\left|V_R^+\right|\angle\theta_{VR}^+=\left|Z_R^+\right|\left|I_{IBR}^+\right|\angle\left(\theta_{VR}^+-\phi^++\theta_Z^+\right)+\left|V_F^+\right|\angle\theta_{VF}^+ \quad (9)$$

where θ_{VF}^+ is the PS voltage angle measured at the fault locations; and θ_Z^+ is the PS impedance angle.

By decomposing (9) into real and imaginary parts and applying trigonometric function properties, $\Delta\theta_{RF}^+$ can be calculated as:

$$\Delta\theta_{RF}^+=\sin^{-1}\left(\frac{\left|Z_R^+\right|\left|I_{IBR}^+\right|}{\left|V_F^+\right|}\sin\left(-\phi^++\theta_Z^+\right)\right) \quad (10)$$

To determine the maximum range of $\Delta\theta_{RF}^+$, $\left|I_{IBR}^+\right|$ is selected equal to the maximum current limit of IBR, i.e., 1.5 p.u. [28], while the maximum value of $\left|Z_R^+\right|$ is determined from the TL design limitations, which should be designed to allow a maximum of 5% voltage regulation at the rated load [26], [27]. Thus, $\left|Z_R^+\right|\approx 0.1$ p.u. while $\theta_Z^+\approx 80°$. Since the IBR injects PS active and reactive currents during faults, ϕ^+ can vary between 0° and 90°. To obtain the maximum range of $\Delta\theta_{RF}^+$, ϕ^+ is set at its limits. i.e., 0° and 90°. In the meanwhile, $\left|V_F^+\right|$ varies according to the value of the fault resistance. Thus, $\Delta\theta_{RF}^+$ is determined at the minimum and maximum value of $\left|V_F^+\right|$ to get the maximum range of $\Delta\theta_{RF}^+$ for different fault resistances. The minimum value of $\left|V_F^+\right|$ occurs at bolted faults, and it differs according to the fault type as follows.

1) For SLG fault, the minimum value of $\left|V_F^+\right|$ is 2/3 p.u.. Thus, for bolted fault, the maximum value of $\Delta\theta_{RF}^+$ in bolted SLG faults changes from –2.3° to 12.5°.

2) For LLG faults, the minimum value of $\left|V_F^+\right|$ = 1/3 p.u.. Thus, for a negligible value of R_{ph}, the maximum variation of $\Delta\theta_{RF}^+$ for bolted LLG faults changes from –4.5° to 26°.

3) For LL faults, the minimum value of $\left|V_F^+\right|$ is 0.5 p.u.. Hence, for bolted LL faults, the range of $\Delta\theta_{RF}^+$ is [–3°, 17.2°].

The maximum value of $\left|V_F^+\right|$ is selected to be 0.9 p.u., which is the threshold for a PS relay to operate. Thus, for high-resistive faults, i.e., high R_g in SLG and high R_{ph} in LL (G) faults, the range of $\Delta\theta_{RF}^+$ is [–1.7°, 9.5°]. Consequently, when the IBR injects a balanced current, the TL effect on the difference between δ_R^+ and δ_F^+, i. e., $\Delta\delta_{RF}^+$, and that between δ_R^0 and δ_F^0, i.e., $\Delta\delta_{RF}^0$, are concluded in Table I.

2) Following New GCs

The controller of IBR is designed to inject both PS and NS currents according to recent GC specifications. Thus, $\Delta\theta_{RF}^-$ and $\Delta\theta_{RF}^+$ are determined by studying the NS and PS circuits, respectively.

In the NS circuit, the IBR is controlled to inject NS current at the IBR terminal, while the conventional power grid can be represented by a constant impedance. Thus, the reduced equivalent SLD of NS circuit can be depicted, as shown in Fig. 10. Hence, the relation between V_R^- and V_F^- resembles (10) determined for the PS circuit, as follows:

TABLE I
RANGES OF $\Delta\delta_{RF}^+$ AND $\Delta\delta_{RF}^0$ IN CONVENTIONAL CONTROLLER

Fault type	R_f	$\Delta\theta_{RF}^-$ (°)	$\Delta\theta_{RF}^+$ (°)	$\Delta\delta_{RF}^+$ (°)	$\Delta\delta_{RF}^0$ (°)
AG	Bolted	0	[–2.3, 12.8]	[–12.8, 2.3]	0
	High R_g	0	[–1.7, 9.5]	[–9.5, 1.7]	0
BCG	Bolted	0	[–4.5, 26.3]	[–26.3, 4.5]	0
	High R_g	0	[–4.5, 26.3]	[–26.3, 4.5]	0
	High R_{ph}	0	[–1.7, 9.5]	[–9.5, 1.7]	0
BC	Bolted	0	[–3, 17.2]	[–17.2, 3]	0
	High R_{ph}	0	[–1.7, 9.5]	[–9.5, 1.7]	0

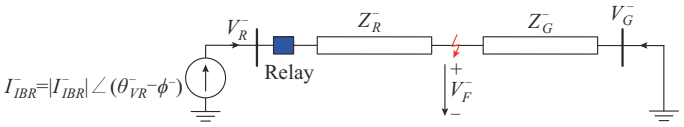

Fig. 10. Equivalent SLD of NS circuit.

$$\left|V_R^-\right|\angle\theta_{VR}^-=\left|Z_R^-\right|\left|I_{IBR}^-\right|\angle\left(\theta_{VR}^--\phi^-+\theta_Z^-\right)+\left|V_F^-\right|\angle\theta_{VF}^- \quad (11)$$

Consequently, the value of $\Delta\theta_{RF}^-$ can be inferred by:

$$\Delta\theta_{RF}^-=\sin^{-1}\left(\frac{\left|Z_R^-\right|\left|I_{IBR}^-\right|}{\left|V_F^-\right|}\sin\left(-\phi^-+\theta_Z^-\right)\right) \quad (12)$$

Recent GCs impose the injection of NS current to reduce unbalanced voltage during asymmetric faults. For instance, the German GC, i. e., VDE-AR-N 4120-GC [29], enforces the IBR to inject NS current according to:

$$I_q^-=K\left|V_R^-\right| \quad (13)$$

where I_q^- is an inductive NS reactive current; and K is a constant that can be selected from the range of [2, 6]. Thus, the maximum NS current is equal to $6\left|V_R^-\right|$, while $\phi^-=-90°$. By substituting $\left|I_{IBR}^-\right|=6\left|V_R^-\right|$, $\phi^-=-90°$, and assuming $\left|V_R^-\right|=\left|V_F^-\right|$ in (12), the maximum value of $\Delta\theta_{RF}^-$ is 5.98°. It is worth mentioning that $\left|V_R^-\right|<\left|V_F^-\right|$. Thus, the actual maximum value of $\Delta\theta_{RF}^-$ is less than 5.98°. The actual maximum value of $\Delta\theta_{RF}^-$ can be determined by substituting $\left|I_{IBR}^-\right|=6\left|V_R^-\right|$, $\phi^-=-90°$, and $Z_R^-=0.1\angle 80°$ in (11) as:

$$\left|V_R^-\right|\angle\theta_{VR}^-=0.6\left|V_R^-\right|\angle\left(\theta_{VR}^-+170°\right)+\left|V_F^-\right|\angle\theta_{VF}^- \quad (14)$$

By solving (14), the actual maximum value of $\Delta\theta_{RF}^-$ is 3.75°, which could be lower at bolted faults because the current is limited to avoid exceeding the maximum current limit. However, this reduction is small; thus, the maximum value of $\Delta\theta_{RF}^-$ is considered equal to 3.75° for both bolted and high-resistive faults, whereas the minimum value is 0° at faults close to the relay location.

Similarly, the PS circuit can be analyzed as in Subsection III-B-1), where the PS current magnitude and power factor are determined from GC requirements. In the German GC, the IBR should inject positive-reactive power according to:

$$I_q^+=K\left|\Delta V_R^+\right| \quad (15)$$

where I_q^+ is a capacitive PS reactive current. In addition, the IBR should inject PS active current to achieve the maximum current limit. Thus, for bolted faults, ϕ^+ is equal to 90° when

$K=6$, but it could be reduced to 70° during SLG faults for $K=2$. At high-resistive faults, i.e., $V_R^-=0.9$ p.u., ϕ^+ is equal to 8.8° and 42° when K is equal to 2 and 6, respectively. It is worth mentioning that $\left|I_{IBR}^+\right|$ is approximately equal to 1.5 p.u. at high-resistive faults, and this value is reduced at low-resistive faults to avoid exceeding the maximum current limit, because the IBR is injecting PS and NS currents simultaneously.

Consequently, for bolted faults, $\Delta\theta_{RF}^+$ approaches its maximum value when $\phi^+=90°$ and $\left|I_{IBR}^+\right|=1.5$ p.u., while the minimum value occurs when $\phi^+=70°$. On the other hand, during high-resistive faults, $\left|\Delta\theta_{RF}^+\right|$ reaches its maximum value when ϕ^+ equals 8.8°. Accordingly, when the IBR is controlled according to new GCs, the TL effects on $\Delta\delta_{RF}^+$ and $\Delta\delta_{RF}^0$ can be summarized, as shown in Table II.

TABLE II
RANGES OF $\Delta\delta_{RF}^+$ AND $\Delta\delta_{RF}^0$ WHEN IBR FOLLOWS NEW GCS

Type	R_f	$\Delta\theta_{RF}^-$ (°)	$\Delta\theta_{RF}^+$ (°)	$\Delta\delta_{RF}^+$ (°)	$\Delta\delta_{RF}^0$ (°)
AG	Bolted	[0, 3.8]	[1.7, −2.3]	[−1.7, 6.1]	[0, 3.8]
	High R_g	[0, 3.8]	[0, 8.6]	[0, −5.1]	[0, 3.8]
BCG	Bolted	[0, 3.8]	[0, −4.5]	[0, 8.3]	[0, 3.8]
	High R_g	[0, 3.8]	[0, −4.5]	[0, 8.3]	[0, 3.8]
	High R_{ph}	[0, 3.8]	[0, 8.6]	[0, −5.1]	[0, 3.8]
BC	Bolted	[0, 3.8]	[0, −3]	[0, 6.8]	
	High R_{ph}	[0, 3.8]	[0, 8.6]	[0, −5.1]	

3) Eliminating Active and Reactive Power Ripples

Active and reactive power ripples introduce challenges in the IBR control and generate oscillations in the direct current (DC) link voltage, which could reduce the lifetime of the DC link capacitor. Thus, some scholars suggest injecting NS current with specific magnitude and angle to eliminate either active or reactive power ripples. However, they do not consider the reliable operation of protection functions in their controllers. The instantaneous active and reactive power can be deduced from the instantaneous PS and NS currents and voltages as follows:

$$p=v_R^+i_R^++v_R^-i_R^-+\underbrace{v_R^-i_R^++v_R^+i_R^-}_{\tilde{P}_{2\omega}} \tag{16a}$$

$$q=v_{\perp R}^+i_R^++v_{\perp R}^-i_R^-+\underbrace{v_{\perp R}^-i_R^++v_{\perp R}^+i_R^-}_{\tilde{Q}_{2\omega}} \tag{16b}$$

where p and q are the instantaneous active and reactive power, respectively; $\tilde{P}_{2\omega}$ and $\tilde{Q}_{2\omega}$ are the oscillating components of active and reactive power at double the nominal frequency, respectively; $v_{\perp R}^+$ is lagging the PS voltage measured at the relay v_R^+ by 90°; and $v_{\perp R}^-$ is leading the NS voltage measured at the relay v_R^- by 90°.

One of the methods to eliminate active power oscillation is obtained by setting $\left|I_{IBR}^-\right|$ and $\angle I_{IBR}^-$ as follows:

$$\begin{cases}\left|I_{IBR}^-\right|=\dfrac{\left|V_R^-\right|}{\left|V_R^+\right|}\left|I_{IBR}^+\right| \\ \angle I_{IBR}^-=\theta_{VR}^--\phi^++180°\end{cases} \tag{17}$$

Consequently, ϕ^- is inferred by:

$$\phi^-=\phi^++180° \tag{18}$$

On the other hand, a method to eliminate reactive power ripples is inferred by calculating $\left|I_{IBR}^-\right|$ and $\angle I_{IBR}^-$ using:

$$\begin{cases}\left|I_{IBR}^-\right|=\dfrac{\left|V_R^-\right|}{\left|V_R^+\right|}\left|I_{IBR}^+\right| \\ \angle I_{IBR}^-=\theta_{VR}^--\theta_{VR}^++\left(\theta_{VR}^+-\phi^+\right)=\theta_{VR}^--\phi^+\end{cases} \tag{19}$$

Hence, ϕ^- should be given by:

$$\phi^-=\phi^+ \tag{20}$$

It can be observed that $\left|I_{IBR}^-\right|$ is the same for active and reactive power ripple elimination; thus, $\Delta\theta_{RF}^-$ for these two control strategies has the same expression. By substituting (17) into (12), $\Delta\theta_{RF}^-$ is formulated by:

$$\Delta\theta_{RF}^-=\sin^{-1}\left(\frac{\left|Z_R^-\right|\left|I_{IBR}^+\right|\left|V_R^-\right|}{\left|V_F^-\right|\left|V_R^+\right|}\sin\left(-\phi^-+\theta_Z^-\right)\right) \tag{21}$$

Since the DG fault current is limited, it is assumed that $\left|V_R^-\right|\approx\left|V_F^-\right|$. Then, by comparing the result with (10), $\Delta\theta_{RF}^-$ and $\Delta\theta_{RF}^+$ are deduced by:

$$\Delta\theta_{RF}^\pm=\sin^{-1}\left(\frac{\left|Z_R^\pm\right|\left|I_{IBR}^+\right|}{\left|V_R^+\right|}\sin\left(-\phi^\pm+\theta_Z^\pm\right)\right) \tag{22}$$

Since IBRs inject PS and NS currents simultaneously, $\left|I_{IBR}^+\right|$ is limited to avoid exceeding the current limit of IBR. By considering current limitations for $\left|I_{IBR}^+\right|$ and $\left|I_{IBR}^-\right|$, $\Delta\theta_{RF}^\pm$ can be formulated by (23), as elaborated in Appendix B.

$$\Delta\theta_{RF}^\pm=\sin^{-1}\left(\frac{1.5\left|Z_R^\pm\right|}{\sqrt{\left|V_R^+\right|^2+\left|V_R^-\right|^2+\left|V_R^+\right|\left|V_R^-\right|}}\sin\left(-\phi^\pm+\theta_Z^\pm\right)\right) \tag{23}$$

Since ϕ^+ ranges between 0° and 90°, ϕ^- varies from 180° to −90° when the system is controlled to eliminate active power ripples. Thus, for bolted faults, $\Delta\theta_{RF}^\pm$ is as follows.

1) For SLG faults, $\left|V_F^+\right|$ = 2/3 p.u.. while $\left|V_F^-\right|$ = 1/3 p.u.. Thus, the range of $\Delta\theta_{RF}^\pm$ is $[\mp1.7°, \pm9.7°]$.

2) For LLG faults, $\left|V_F^\pm\right|$ = 1/3 p.u.. Thus, the range of $\Delta\theta_{RF}^\pm$ is $[\mp2.6°, \pm14.9°]$.

3) For LL faults, $\left|V_F^\pm\right|$ = 1/2 p.u.. Thus, the range of $\Delta\theta_{RF}^\pm$ is $[\mp1.8°, \pm9.9°]$.

Nevertheless, during high-resistive faults, i.e., $\left|V_F^+\right|$ = 0.9 p.u., $\Delta\theta_{RF}^\pm$ will vary from $\mp1.6°$ to $\pm9.1°$.

On the other hand, ϕ^- for eliminating reactive power ripples varies from 0° to 90°. Thus, $\Delta\theta_{RF}^-$ is equal to $\Delta\theta_{RF}^+$, and the effect of the TL on $\Delta\delta_{RF}^+$ can be neglected.

Table III and Table IV summarize the TL effects on $\Delta\delta_{RF}^+$ and $\Delta\delta_{RF}^0$ when the IBR is controlled to eliminate active and reactive power ripples. It can be inferred that the elimination of active power ripple can affect $\Delta\delta_{RF}^+$ significantly, e.g., −30° in LLG faults with high R_g. On the other hand, $\Delta\delta_{RF}^0$ can vary from −15° to 15° according to the controller type. These significant phase shifts can affect the performance of PSMs and should be taken into consideration when designing PSM zones.

TABLE III
RANGES OF $\Delta\delta^{+}_{RF}$ AND $\Delta\delta^{0}_{RF}$ WHEN IBR IS CONTROLLED TO ELIMINATE ACTIVE POWER RIPPLES

Fault type	R_f	$\Delta\theta^{-}_{RF}$ (°)	$\Delta\theta^{+}_{RF}$ (°)	$\Delta\delta^{+}_{RF}$ (°)	$\Delta\delta^{0}_{RF}$ (°)
AG	Bolted	[−9.7, −1.7]	[9.7, 1.7]	[−19.4, 3.4]	[−9.7, 1.7]
	High R_g	[−9.1, −1.6]	[9.1, 1.6]	[−18.2, 3.2]	[−9.1, 1.6]
BCG	Bolted	[−14.9, −2.6]	[14.9, 2.6]	[−29.8, 5.2]	[−14.9, 2.6]
	High R_g	[−14.9, −2.6]	[14.9, 2.6]	[−29.8, 5.2]	[−14.9, 2.6]
	High R_{ph}	[−9.1, −1.6]	[9.1, 1.6]	[−18.2, 3.2]	[−9.1, 1.6]
BC	Bolted	[−9.9, −1.8]	[9.9, 1.8]	[−19.8, 3.6]	
	High R_{ph}	[−9.1, −1.6]	[9.1, 1.6]	[−18.2, 3.2]	

TABLE IV
RANGES OF $\Delta\delta^{+}_{RF}$ AND $\Delta\delta^{0}_{RF}$ WHEN IBR IS CONTROLLED TO ELIMINATE REACTIVE POWER RIPPLES

Fault type	R_f	$\Delta\theta^{-}_{RF}$ (°)	$\Delta\theta^{+}_{RF}$ (°)	$\Delta\delta^{+}_{RF}$ (°)	$\Delta\delta^{0}_{RF}$ (°)
AG	Bolted	[−1.7, 9.7]	[−1.7, 9.7]	[0, 0]	[−1.7, 9.7]
	High R_g	[−1.6, 9.1]	[−1.6, 9.1]	[0, 0]	[−1.6, 9.1]
BCG	Bolted	[−2.6, 14.9]	[−2.6, 14.9]	[0, 0]	[−2.6, 14.9]
	High R_g	[−2.6, 14.9]	[−2.6, 14.9]	[0, 0]	[−2.6, 14.9]
	High R_{ph}	[−1.6, 9.1]	[−1.6, 9.1]	[0, 0]	[−1.6, 9.1]
BC	Bolted	[−1.8, 9.9]	[−1.8, 9.9]	[0, 0]	
	High R_{ph}	[−1.6, 9.1]	[−1.6, 9.1]	[0, 0]	

IV. PROPOSED PSM

According to the analysis conducted in Sections II and III, the ranges for δ^{+}_{R} and δ^{0}_{R} are determined to allow accurate PSM for different fault resistances, IBR controllers, and fault locations. First, δ^{+}_{F} and δ^{0}_{F} are determined for bolted and high-resistive faults, as illustrated in Section II. Then, full ranges of $\Delta\delta^{+}_{RF}$ and $\Delta\delta^{0}_{RF}$ are determined for bolted and high-resistive faults, respectively, by selecting the maximum and minimum shifts deduced from Section III for different IBR controllers. Hence, the full range of δ^{+}_{R} and δ^{0}_{R} for bolted and high-resistive faults are determined individually, as shown in Table V. Lastly, the ranges of δ^{+}_{R} and δ^{0}_{R} are deduced by combing the results from bolted and high-resistive faults, as presented in Table V.

A. δ^{0}_{R} Zones

It can be deduced that δ^{0}_{R} for AG and BCG faults can vary from −10° to 10° and from −88° to 10°, respectively; thus, these zones can be combined. Then, by extending the zone width to 120°, δ^{0}_{R} zones for AG and BCG faults range from −95° to 25°. Subsequently, BG and CAG faults can be determined by shifting the BG/CAG zone by −120°, while CG and ABG are deduced by shifting the BG/CAG zones by 120°. The proposed δ^{0}_{R} zones are depicted in Fig. 11.

TABLE V
RANGES OF δ^{+}_{R} AND δ^{0}_{R} FOR FAULTS FED BY IBR

Fault type	R_f	$\Delta\delta^{+}_{RF}$ (°)	$\Delta\delta^{0}_{RF}$ (°)	δ^{+}_{F} (°)	δ^{0}_{F} (°)	δ^{+}_{R} (°)	δ^{0}_{R} (°)	δ^{+}_{R} (full range) (°)	δ^{0}_{R} (full range) (°)
AG	Bolted	[−20, 6]	[−10, 10]	−180	0	[−200, −174]	[−10, 10]	[−200, −96]	[−10, 10]
	High	[−19, 4]	[−10, 10]	−100	0	[−119, −96]	[−10, 10]		
BCG	Bolted	[−30, 9]	[−15, 15]	0	0	[−30, 9]	[−15, 15]		
	High R_g	[−30, 9]	[−15, 15]	0	−73	[−30, 9]	[−88, −65]	[30, 72]	[−88, 10]
	High R_{ph}	[−19, 4]	[−10, 10]	68	0	[49, 72]	[−10, 10]		
BC	Bolted	[−20, 7]		0		[−20, 7]		[20, 72]	
	High	[−19, 4]		68		[49, 76]			

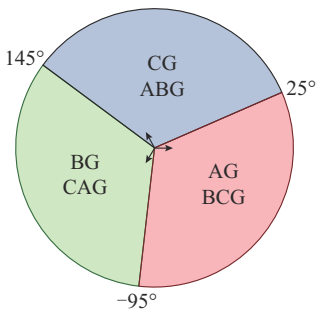

Fig. 11. Proposed δ^{0}_{R} zones.

B. δ^{+}_{R} Zones

It can be observed from Table V that δ^{+}_{R} for AG and BC(G) faults are different and cannot be combined. Thus, the zones for AG and BC(G) faults are constructed separately. For an AG fault, δ^{+}_{R} zones range between −200° and −96°. Thus, by extending the zone to 120°, the range of δ^{+}_{R} zones is from −210° to −90°. Hence, δ^{+}_{R} zones for SLG faults are determined as shown in Fig. 12(a), by shifting the AG zone by 120° and −120° for CG and BG faults, respectively. On the other hand, δ^{+}_{R} zones for BC and BCG faults can be united and the range is from −40° to 80°. Lastly, LL(G) zones for δ^{+}_{R} is inferred as depicted in Fig. 12(b), where AB(G) and CA(G) are determined by shifting BC(G) zone by −120° and 120°, respectively.

C. Pinpoint Fault Type

First, δ^{0}_{R} is compared with its proposed zones; thus, two types of faults, e.g., AG and BCG, can be determined. Thereafter, δ^{+}_{R} is used to differentiate between SLG and LLG faults. Hence, the fault type is pinpointed, e.g., if δ^{+}_{R} is within the AG zone; then, an AG fault is identified, but if it is located in the BCG zone; then, a BCG fault is determined. The two types of faults determined by δ^{0}_{R} zones have different zones when using δ^{+}_{R}. Thus, the fault type can be determined effectively.

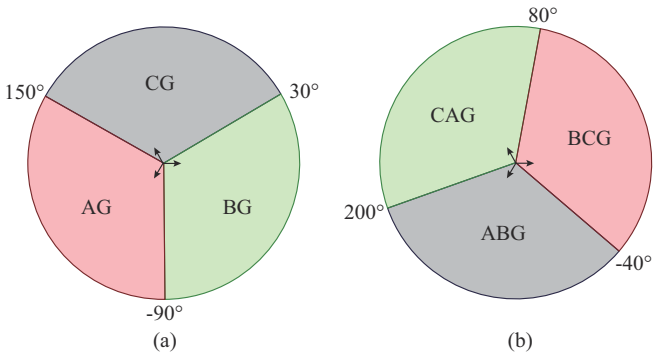

Fig. 12. Proposed δ_R^+ zones. (a) SLG zones. (b) LL(G) zones.

V. Performance Evaluation

The accuracy of the fault analysis and the effectiveness of the proposed PSM are verified using PSCAD/EMTDC simulations, which are carried out for several fault locations, resistances, types, and IBR controllers. Figure 13 represents a 230 kV 60 Hz transmission system that comprises a 50 MVA IBR and three voltage sources [17]. The PS and ZS impedances for the voltage sources are as follows: $Z_{s1}^+ = 12.66\angle 83°\ \Omega$, $Z_{s1}^0 = 11.1\angle 83°\ \Omega$, $Z_{s3}^+ = 7.76\angle 81°\ \Omega$, $Z_{s3}^0 = 5\angle 81°\ \Omega$, $Z_{s4}^+ = 12.7\angle 84°\ \Omega$, and $Z_{s4}^0 = 11.2\angle 84°\ \Omega$, respectively, where the subscripts 1, 3, and 4 represent the number of buses connected to a source. The IBR is integrated into bus 2 through a 100 MVA, 22 kV/230 kV delta/star-grounding transformer. The PS impedance of TLs is $Z_{TL}^+ = (0.0895 + j0.508)\Omega$/km, while the ZS impedance $Z_{TL}^0 = (0.1791 + j1.015)\Omega$/km. Moreover, the TL lengths for L_{15}, L_{25}, L_{35}, and L_{45} are 155, 100, 110, and 120 km, respectively.

A. Compatibility with Conventional Controllers

Table VI reports the values of δ^+ and δ^0 measured at the relay and fault locations, and illustrates the TL effects on the phase shifts between δ_R^+, δ_R^0 and δ_F^+, δ_F^0, respectively, when the IBR is controlled to inject active PS current. The results in Table VI verify the accuracy of the mathematical analysis where the TL has a negligible effect on $\Delta\delta_{RF}^0$ when the IBR follows conventional controllers. Furthermore, injecting PS active current produces a negative value of $\Delta\delta_{RF}^+$, whose angle depends on fault conditions. Increasing the distance between the fault and relay locations increases the value of $|\Delta\delta_{RF}^+|$. For instance, during a bolted BC fault, $\Delta\delta_{RF}^+$ is equal to −8.4° and −5.2° for faults at bus B5 and in the middle of L_{25}, respectively. Moreover, the value of $|\Delta\delta_{RF}^+|$ is inversely proportional to $|V_F^+|$, e.g., $\Delta\delta_{RF}^+$ is equal to −12.5° and −24.9° for bolted AG and BCG faults at bus B5, respectively, where $|V_F^+| \approx 0.67$ p.u. and 0.33 p.u., respectively. Further, $\Delta\delta_{RF}^+ =$ −12.5° and −9.2° for bolted and high-resistive AG faults, respectively, where $|V_F^+| \approx 0.33$ p.u. and 0.9 p.u., respectively. In addition, Table VI confirms the correctness of the proposed zones in determining the fault type accurately, where δ_R^+ and δ_R^0 are settled in their corresponding fault type zones, respectively. For example, δ_R^+ and δ_R^0 are equal to 64.3° and 6.2°, respectively, for a BCG fault at bus 5 with $R_{ph} = 40\ \Omega$. It is worth noting that the proposed PSM is tested at negligible and immense resistive faults, i.e., R_g and R_{ph}, to ensure that any other values of R_g and R_{ph} will not affect the accuracy of the proposed PSM.

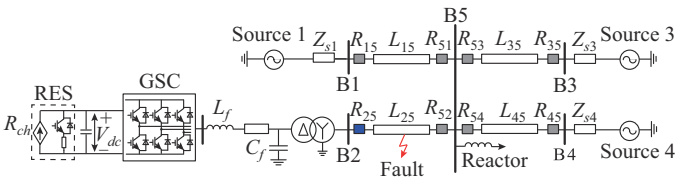

Fig. 13. SLD of test system.

TABLE VI
Active Power Generation when IBR Follows Conventional Controller

Fault type	R_g (Ω)	R_{ph} (Ω)	Fault at 50% of L_{25}						Fault at bus B5					
			δ_F^+ (°)	δ_R^+ (°)	$\Delta\delta_{RF}^+$ (°)	δ_F^0 (°)	δ_R^0 (°)	$\Delta\delta_{RF}^0$ (°)	δ_F^+ (°)	δ_R^+ (°)	$\Delta\delta_{RF}^+$ (°)	δ_F^0 (°)	δ_R^0 (°)	$\Delta\delta_{RF}^0$ (°)
AG	0		180.0	173.3	−6.7	0.0	0.0	0.0	180.3	167.8	−12.5	0.0	0.0	0.0
	50		−127.6	−130.9	−3.3	0.3	0.4	0.1	−118.7	−126.3	−7.6	0.2	0.5	0.3
BCG	0	0	0.0	−14.7	−14.7	0.0	0.0	0.0	0.0	−24.9	−24.9	0.0	−0.1	−0.1
	0	40	61.1	55.5	−5.6	−6.5	−6.5	0.0	73.1	64.3	−8.8	5.6	6.2	0.6
	50	0	0.0	−9.0	−9.0	−66.3	−66.0	0.0	0.0	−17.9	−17.9	−68.9	−69.0	−0.1
BC		0	0.0	−8.6	−8.6				0.0	−17.4	−17.4			
		40	55.3	50.1	−5.2				67.0	58.6	−8.4			

Table VII demonstrates the effect of conventional controller of IBR on the values of $\Delta\delta_{RF}^+$ and $\Delta\delta_{RF}^0$ when the controller injects reactive PS current, and verifies the accuracy of the proposed zones. In light of the results, the accuracy of the proposed short-circuit analysis is assured. Similar to Table VI, $\Delta\delta_{RF}^0$ is 0°, while $\Delta\delta_{RF}^+$ has a positive value. The values of $\Delta\delta_{RF}^+$ increases for far faults, e.g., $\Delta\delta_{RF}^+$ is 0.8° and 2.3° for faults at 10% and 50% of L_{25}, respectively. However, increasing $|V_F^+|$ decreases $\Delta\delta_{RF}^+$. For illustration, $\Delta\delta_{RF}^+ = 0.2°$, 1°, 1.4°, and 2.3° when $|V_F^+| \approx 0.9$, 0.67, 0.5, and 0.3 p.u., respectively, for faults at 50% of L_{25}. Further, it can be deduced that δ_R^+, δ_R^0, δ_F^+, and δ_F^0 fall correctly in their fault type zones. For instance, for a BG fault at 50% of L_{25} and $R_g = 50\ \Omega$, $\delta_R^+ = -8.5°$ and $\delta_R^0 = -120°$, which settle in their correct zones, respectively. It is worth mentioning that at a high value of R_g, δ_F^0 is almost similar to a bolted fault condition, while δ_F^+ is shifted by about 60°, as explained in the short-circuit analysis.

TABLE VII
REACTIVE POWER GENERATION WHEN IBR FOLLOWS CONVENTIONAL CONTROLLER

Fault type	R_g (Ω)	R_{ph} (Ω)	Fault at 10% of L_{25}						Fault at 50% of L_{25}					
			δ_F^+ (°)	δ_R^+ (°)	$\Delta\delta_{RF}^+$ (°)	δ_F^0 (°)	δ_R^0 (°)	$\Delta\delta_{RF}^0$ (°)	δ_F^+ (°)	δ_R^+ (°)	$\Delta\delta_{RF}^+$ (°)	δ_F^0 (°)	δ_R^0 (°)	$\Delta\delta_{RF}^0$ (°)
BG	0		−60.0	−59.8	0.2	−120	−120	0	−60.0	−59.0	1.0	−120.0	−120	0.0
	50		−8.6	−8.5	0.1	−120	−120	0	−8.6	−8.5	0.1	−120.0	−120	−0.1
CAG	0	0	120.0	120.8	0.8	−120	−120	0	120.0	122.3	2.3	−120.0	−120	0.0
	0	40	169.0	169.6	0.2	−148	−148	0	−178.9	−178.0	0.9	−127.0	−127	0.0
	50	0	120.0	120.3	0.3	167	167	0	120.0	121.5	1.5	173.7	174	0.0
CA		0	120.0	120.3	0.3				120.0	121.4	1.4			
		40	168.0	168.1	0.2				175.3	176.1	0.8			

Figure 14 demonstrates a case study from Tables VI and VII to ensure the accuracy of the proposed PSM.

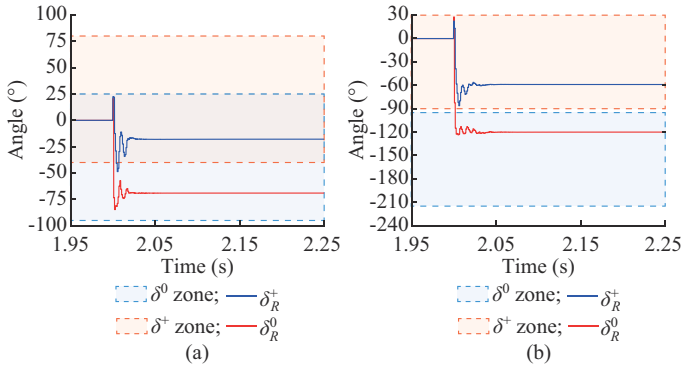

Fig. 14. Performance of proposed PSM during conventional controller. (a) A BCG fault at bus B5. (b) A BG fault at 50% of L_{25}.

Figure 14(a) represents a BCG fault at bus B5 when the IBR injects a unity power factor current. The results show that both δ_R^+ and δ_R^0 settle correctly within the proposed zones in less than half a cycle. In addition, δ_R^+ and δ_R^0 are placed in their zones with adequate margins from their zone limits, i.e., about 25°. On the other hand, Fig. 14(b) exhibits the results for a bolted BG fault at 50% of L_{25} when the IBR is injecting reactive current. The results show that δ_R^+ and δ_R^0 are placed in their correct zones under both transient and steady-state conditions, in which δ_R^+ is settled at −59°, while δ_R^0 is settled at −120°, which is almost equal to the mathematical results for a bolted BG fault.

B. Compatibility with Recent GCs

In this subsection, the precision of the proposed PSM when the IBR is controlled to follow the new German GC is validated. Moreover, the correctness of the mathematical analysis, which studies the TL effect on $\Delta\delta_{RF}^+$ and $\Delta\delta_{RF}^0$, is confirmed. Table VIII displays the values of δ_R^+, δ_R^0, δ_F^+, δ_F^0, $\Delta\delta_{RF}^+$, and $\Delta\delta_{RF}^0$ when $K=6$ for faults at 50% of L_{25} and bus B5. All the values of δ_R^+ and δ_R^0 demonstrated in Table VIII lay in the proposed zones correctly with the minimum margins of 10° and 25° for δ_R^+ and δ_R^0, respectively. For instance, when an ABG fault occurs at bus B5 with $R_{ph}=20$ Ω, δ_R^+ is −51.9° and δ_R^0 is 133°, which are placed in their correct fault type zones. On the other hand, the zones proposed in [18] fail to determine the fault type properly. The results show that the value of $\Delta\delta_{RF}^0$ is positive and varies between 1.7° to 3.6°, which coincides with the analysis in Subsection III-B-2). Moreover, $\Delta\delta_{RF}^+$ has positive values for bolted faults and ranges from 4.2° to 6.2° for faults at bus B5. Meanwhile, $\Delta\delta_{RF}^+$ is negative for SLG faults when $R_g=50$ Ω. For instance, $\Delta\delta_{RF}^+=-0.8°$ and −2.5° for a CG fault at 50% of L_{25} and bus B5, respectively. However, $\Delta\delta_{RF}^+$ is positive for high-resistive LLG faults because the fault resistance is not sufficient to enforce the IBR to inject active PS current.

TABLE VIII
IBR CONTROLLER FOLLOWING GERMAN GC WHEN $K=6$

Fault type	R_g (Ω)	R_{ph} (Ω)	Fault at 50% of L_{25}						Fault at bus B5					
			δ_F^+ (°)	δ_R^+ (°)	$\Delta\delta_{RF}^+$ (°)	δ_F^0 (°)	δ_R^0 (°)	$\Delta\delta_{RF}^0$ (°)	δ_F^+ (°)	δ_R^+ (°)	$\Delta\delta_{RF}^+$ (°)	δ_F^0 (°)	δ_R^0 (°)	$\Delta\delta_{RF}^0$ (°)
CG	0		61.0	63.5	2.5	122.0	123.7	1.7	60.5	64.8	4.3	121.0	124.0	3.0
	50		117.4	116.6	−0.8	122.0	123.7	1.7	123.2	120.7	−2.5	121.0	125.0	3.6
ABG	0	0	−120.0	−116.0	3.7	120.0	121.7	1.7	−120.0	−113.8	6.2	120.0	123.0	2.8
	0	20	−67.5	−64.6	2.9	122.0	123.5	1.7	−56.4	−51.9	4.5	130.0	133.0	3.0
	50	0	−120.0	−117.0	2.9	53.7	55.4	1.7	−120.0	−115.1	4.9	51.1	53.9	2.8
AB		0	−120.0	−117.0	2.8				−120.0	−115.2	4.8			
		20	−76.7	−74.2	2.5				−64.7	−60.6	4.1			

Table IX displays the measured values of δ^+ and δ^0 at the relay and fault locations when $K=2$. It can be deduced that $\Delta\delta_{RF}^0$ has a positive value, and it is affected by the fault location. For instance, $\Delta\delta_{RF}^0=0.3$ and 0.8 p.u. for bolted CAG faults at 10% and 50% of L_{25}, respectively. In addition, $\Delta\delta_{RF}^0$ is almost constant, i.e., $\Delta\delta_{RF}^0\approx 0.8°$, in spite of various

fault resistances and types, because the IBR current does not exceed its maximum thermal limit. Nevertheless, the value of $\Delta\delta_{RF}^{+}$ is affected by fault location and resistance. For high-resistive faults, i.e., $R_g = 50\ \Omega$ and $R_{ph} = 20\ \Omega$ for SLG and LL(G) faults, respectively, $\Delta\delta_{RF}^{+}$ is negative because the IBR current is mainly composed of active current components. On the other hand, for bolted faults at 50% of L_{25}, it can be observed that $\Delta\delta_{RF}^{+}$ is equal to −1.7° for SLG faults, and 2.3° and 1.4° for LLG and LL faults, respectively, which is in accordance with the theoretical analysis. The difference in the signs of $\Delta\delta_{RF}^{+}$ for SLG and LL(G) bolted faults when $K = 2$ occurs because ΔV^{+} is small during SLG faults; thus, I_q^{+} is small and the IBR can inject an active PS current that is responsible for the negative sign. However, for LL and LLG bolted faults, ΔV^{+} is sufficient to enforce the IBR to inject only PS reactive current, which leads to a positive value of $\Delta\delta_{RF}^{+}$ like the values determined from the mathematical analysis. The results, also, assert the accuracy of the chosen fault type zones as all angles lay in their respective zones.

TABLE IX
IBR CONTROLLER FOLLOWING GERMAN GC WHEN $K = 2$

Fault type	R_g (Ω)	R_{ph} (Ω)	Fault at 10% of L_{25}						Fault at 50% of L_{25}					
			δ_F^{+} (°)	δ_R^{+} (°)	$\Delta\delta_{RF}^{+}$ (°)	δ_F^{0} (°)	δ_R^{0} (°)	$\Delta\delta_{RF}^{0}$ (°)	δ_F^{+} (°)	δ_R^{+} (°)	$\Delta\delta_{RF}^{+}$ (°)	δ_F^{0} (°)	δ_R^{0} (°)	$\Delta\delta_{RF}^{0}$ (°)
BG	0		−59.5	−59.4	0.1	−118	−118	0.2	−59.4	−61.1	−1.7	−119	−118.0	0.8
	50		−3.5	−4.0	−0.5	−118	−118	0.1	−5.2	−8.2	−3.0	−119	−118.0	0.8
CAG	0	0	120.0	120.8	0.8	−120	−120	0.2	120.0	122.3	2.3	−120	−119.0	0.8
	0	20	161.5	161.1	−0.4	−142	−141	0.2	168.2	166.0	−2.2	−122	−121.0	0.7
	50	0	120.0	120.4	0.4	167	168	0.2	120.0	121.5	1.5	174	174.5	0.8
CA		0	120.0	120.3	0.3				120.0	121.4	1.4			
		20	152.2	152.0	−0.2				158.5	157.3	−1.2			

Figure 15(a) and (b) exhibits a case study from Tables VIII and IX, respectively, for faults at 50% of L_{25} when the IBR is controlled to follow the new German GC. Figure 15 (a) presents the results for a CG fault when $K = 6$. The values of δ_R^{+} and δ_R^{0} are equal to 116.6° and 123.7°, respectively, which are in their corresponding fault type zones. In addition, it can be observed that the PSM can determine the fault type in less than half a cycle from the fault inception. On the other hand, Fig. 15(b) displays the results when $K = 2$. δ_R^{+} and δ_R^{0} are placed inside their correct zone and away from the zone limits by about 30° and 20°, respectively.

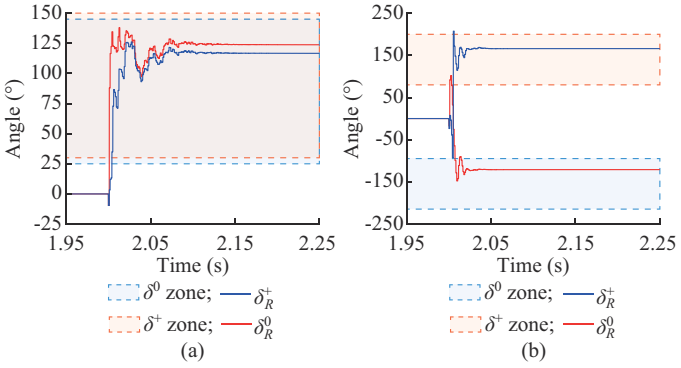

Fig. 15. Performance of proposed PSM when IBR follows new German GC for a fault at 50% of L_{25}. (a) A CG fault. (b) A CAG fault.

C. Compatibility with Elimination of Active and Reactive Power Ripples

In this subsection, the mathematical analysis and the accuracy of proposed PSM are verified when the IBR is controlled to eliminate either active or reactive power ripples. Table X displays the measured angles for faults that take place on bus B5 when the IBR is injecting PS active current and eliminating either active or reactive power ripples. It can be observed from Table X that $|\Delta\delta_{RF}^{0}|$ has almost the same value in the elimination cases of both the active and reactive power ripples, but they have opposite signs for $\Delta\delta_{RF}^{0}$. For example, $\Delta\delta_{RF}^{0}$ is equal to −8.3° and 8.5°, when the IBR is controlled to eliminate active and reactive power ripples for a bolted AG fault, respectively. This is because ϕ^{-} is equal to $\phi^{+} + 180°$ and ϕ^{+} for the elimination of active and reactive power ripples, respectively. In addition, the measured values match theoretical calculation results, e.g., the maximum calculated value of $|\Delta\delta_{RF}^{0}|$ in LLG is equal to 14.9°, which is slightly higher than the measured value 13.7°. This small difference is expected because the mathematical calculations are determined when the angle difference between θ_V^{+} and θ_V^{-} produces the maximum $|I_{IBR}^{+}|$.

In addition, the results verify the accuracy of the calculated values of $\Delta\delta_{RF}^{+}$ in elimination of both active and reactive power ripples. For instance, $\Delta\delta_{RF}^{+}$ is almost equal to 0° for elimination of reactive power ripple, and equals a negative value that varies according to the fault type and resistance when the IBR is controlled to eliminate active power ripples. For example, for a BCG fault when the IBR is injecting active current and eliminating active power ripples, $\Delta\delta_{RF}^{+}$ is equal to −24.6°, −15.3°, and −18.5° for bolted, $R_{ph} = 40\ \Omega$, and $R_g = 50\ \Omega$, respectively. Furthermore, the measured values of δ_R^{+} and δ_R^{0} are placed correctly in their fault type zones. For example, δ_R^{+} and δ_R^{0} are equal to −18.5° and −77.8°, respectively, for a BCG fault with $R_g = 50\ \Omega$.

Table XI demonstrates the results when the IBR injects reactive current and eliminates active or reactive power ripples. It can be observed that $\Delta\delta_{RF}^{0}$ and $\Delta\delta_{RF}^{+}$ shown in Table XI are opposite in sign compared with the results in Table X, which are in accordance with the mathematical analysis.

In light of the results of a bolted AG fault, $\Delta\delta^0_{RF}$ is equal to 1.3° and −1.5° for elimination of active and reactive power ripples, respectively, which are slightly smaller than the maximum values determined by mathematical analysis, i.e., 1.7° and −1.7°, respectively. Further, $\Delta\delta^+_{RF}$ is equal to 0 in elimination of reactive power ripples, which is in accordance with mathematical analysis. Moreover, $\Delta\delta^+_{RF}=2.6°$, which is slightly lower than the maximum shift calculated by mathematical analysis, i.e., 3.4°. Moreover, the results verify the accuracy of the proposed zones in determining the fault type accurately.

TABLE X
ELIMINATION OF ACTIVE AND REACTIVE POWER RIPPLES WHEN PS CURRENT IS INJECTING ACTIVE CURRENT

Fault type	R_g (Ω)	R_{ph} (Ω)	Elimination of active power ripples						Elimination of reactive power ripples					
			δ^+_F (°)	δ^+_R (°)	$\Delta\delta^+_{RF}$ (°)	δ^0_F (°)	δ^0_R (°)	$\Delta\delta^0_{RF}$ (°)	δ^+_F (°)	δ^+_R (°)	$\Delta\delta^+_{RF}$ (°)	δ^0_F (°)	δ^0_R (°)	$\Delta\delta^0_{RF}$ (°)
AG	0		177.9	160.9	−17.0	−3.7	−11.9	−8.2	182.4	182.4	0.0	4.2	12.6	8.4
	50		−123.0	−132.5	−9.8	−3.8	−10.5	−6.7	−116.0	−116.0	−0.2	3.6	10.7	7.1
BCG	0	0	0.0	−24.6	−24.6	0.0	−11.7	−11.7	0.0	0.0	0.0	0.0	13.7	13.7
	0	40	68.3	53.0	−15.3	4.0	−3.5	−7.5	74.0	73.9	−0.1	8.8	17.0	8.2
	50	0	0.0	−18.5	−18.5	−68.9	−77.8	−8.9	0.0	0.0	0.0	−68.9	−58.9	10.0
BC		0	0.0	−18.2	−18.2				0.0	0.0	0.0			
		40	61.7	47.0	−14.7				67.5	67.4	−0.1			

TABLE XI
ELIMINATION OF ACTIVE AND REACTIVE POWER RIPPLES WHEN PS CURRENT IS INJECTING REACTIVE CURRENT

Fault type	R_g (Ω)	R_{ph} (Ω)	Elimination of active power ripples						Elimination of reactive power ripples					
			δ^+_F (°)	δ^+_R (°)	$\Delta\delta^+_{RF}$ (°)	δ^0_F (°)	δ^0_R (°)	$\Delta\delta^0_{RF}$ (°)	δ^+_F (°)	δ^+_R (°)	$\Delta\delta^+_{RF}$ (°)	δ^0_F (°)	δ^0_R (°)	$\Delta\delta^0_{RF}$ (°)
CG	0		60.4	63.7	3.3	120.6	121.9	1.3	59.6	59.6	0.0	119.3	117.8	−1.5
	50		102.4	104.9	2.5	120.5	121.5	1.0	100.3	100.3	0.0	119.3	117.8	−1.5
ABG	0	0	−120.0	−115.6	4.4	120.0	121.5	1.5	−120.0	−119.9	0.1	120.0	117.7	−2.3
	0	40	−48.1	−45.3	2.8	127.3	128.4	1.1	−51.0	−51.0	0.0	123.8	122.3	−1.5
	50	0	−120.0	−116.4	3.6	51.1	52.3	1.2	−120.0	−119.9	0.1	65.3	63.5	−1.8
AB		0	−120.0	−116.7	3.3				−120.0	−120.0	0.0			
		40	−55.0	−52.8	2.2				−57.3	−57.3	0.0			

Figure 16(a) displays a sample result from Table X for a BCG fault with $R_{ph}=40$ Ω when the IBR injects active current and eliminates reactive power ripples. δ^0_R settles at 17° because $\Delta\delta^0_{RF}=9°$, as shown in Table X.

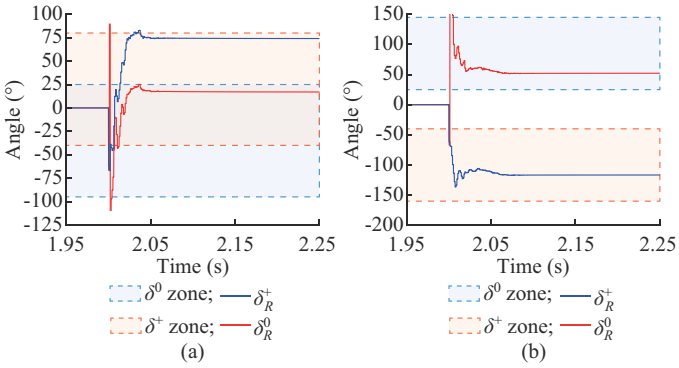

Fig. 16. Performance of proposed PSM for a fault at bus B5 during active and reactive power ripples. (a) A BCG fault. (b) An ABG fault.

This verifies the accuracy of both the mathematical analysis and fault type zones. As shown in Fig. 16(a), δ^+_R settles in its correct zone at 73.9° with a 6° margin from its limit. It is worth noting that zones in [18] fail to determine this fault type properly. On the other hand, Fig. 16(b) reveals the dynamics of a sample case study from Table XI for an ABG fault with $R_g=50$ Ω, when the IBR injects reactive current and eliminates active power ripples. The results verify the accuracy of the proposed zones in determining the fault type while eliminating the active and reactive power ripples. For instance, $\delta^+_R=-116.4°$ and $\delta^0_R=52.3°$, respectively, which lay in their correct fault type zones. In addition, the proposed PSM determines the fault type in less than half a cycle.

D. Comparison with Other PSMs

In this subsection, the proposed PSM is compared against other methods from the literature to substantiate its superiority in detecting faulty phase(s) in transmission systems. Figure 17 displays the results of the PSM measurements during an AG fault at 90% of L_{25} with $R_g=30$ Ω when the IBR is controlled to eliminate active power ripples. As observed in Fig. 17(a)-(c), δ^0_R is placed in its correct zone; however, δ^+_R settles outside the correct zone for an AG fault, leading to incorrect fault classification. On the other hand, Fig. 17(d) validates the accuracy of the proposed PSM in which both δ^0_R and δ^+_R settle inside the proper PSM zone, leading to precise PSM.

Figure 18 exhibits the results of PSM measurements during a BCG fault at 90% of L_{25} with $R_g=15$ Ω when the IBR follows recent GCs [29]. In Fig. 18(a), both δ^0_R and δ^+_R calculated according to [21] fall short in settling inside the BCG zones. Similarly, the adaptive zones in [22], as shown in Fig. 18(b), fail to maintain δ^0_R and δ^+_R inside the BCG adapt-

ed zones, causing a failure in detecting the faulty phase correctly. In Fig. 18(c), δ_R^+ calculated based on [23] has slightly exceeded the maximum zone boundary, resulting in inaccurate detection of the faulty phases. On the contrary, the proposed PSM has successfully detected the faulty phases, as both δ_R^0 and δ_R^+ are placed inside their correct zones, as displayed in Fig. 18(d). These results verify the accurate operation of the proposed PSM in transmission systems compared with other methods in the literature.

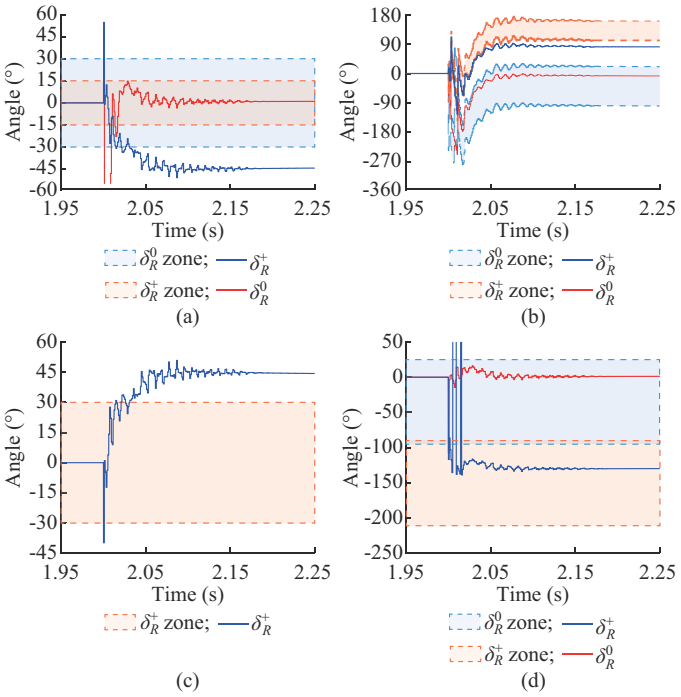

Fig. 17. PSM measurements during an AG fault at 90% of L_{25}. (a) Method in [21]. (b) Method in [22]. (c) Method in [23]. (d) Proposed PSM.

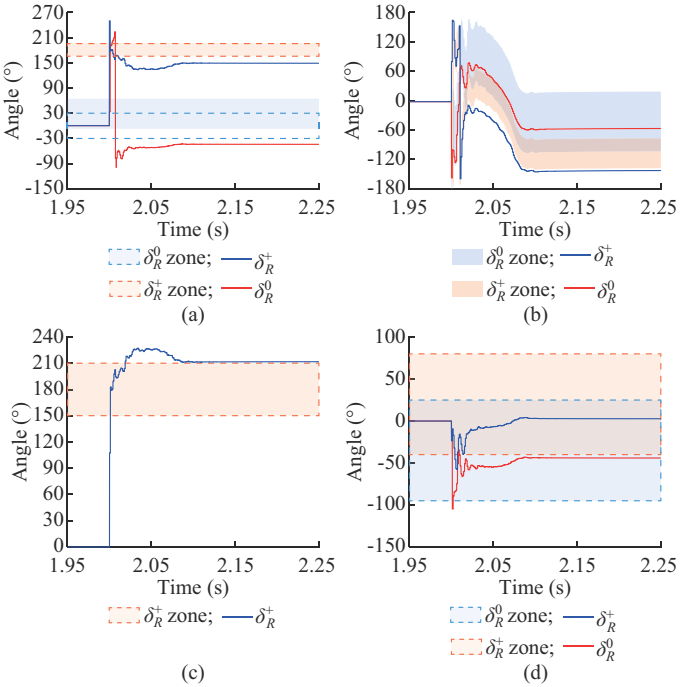

Fig. 18. PSM measurements during a BCG fault at 90% of L_{25}. (a) Method in [21]. (b) Method in [22]. (c) Method in [23]. (d) Proposed PSM.

VI. Conclusion

PSM is a prerequisite element for main protection functions and for new controllers that emulate SG fault currents, though existing PSMs may operate improperly when fault currents are fed by IBRs. In this paper, the root causes for the failure of the PSM based on the relative angles between sequence voltages measured at relay locations, i.e., δ_R^0 and δ_R^+, are elaborated. First, short-circuit analysis at the fault location is investigated to determine the relative angles between sequence voltages measured at fault locations, i.e., δ_F^0 and δ_F^+. Then, δ_R^0 and δ_R^+ are deduced by analyzing the TL effects on the angle difference between sequence voltages measured at the relay and fault locations. Further, new zones of PSM are designed to guarantee precise fault type identification for different fault resistances. Simulation studies substantiate the effectiveness of the proposed PSM with different IBR controllers and fault conditions. Future work could investigate the applicability of using machine learning methods in determining the faulty phase accurately for various IBR control strategies while taking into consideration the TL impact on PSM accuracy.

Appendix A

By analyzing the sequence network for a BCG fault shown in Fig. 4, the sequence voltages are inferred as:

$$\begin{cases} V_F^- = V_x + I_F^- R_{ph} \\ V_F^0 = V_x + I_F^0\left(R_{ph} + 3R_g\right) \\ V_F^+ = V_x + I_F^+ R_{ph} \end{cases} \tag{A1}$$

The relations between sequence currents and their corresponding voltages are given by:

$$\begin{cases} I_F^- = -\dfrac{V_F^-}{Z_{th}^-} \\ I_F^0 = -\dfrac{V_F^0}{Z_{th}^0} \\ I_F^+ = \dfrac{V_F^-}{Z_{th}^-} + \dfrac{V_F^0}{Z_{th}^0} \end{cases} \tag{A2}$$

Thus, using (A1) and (A2), V_F^-, V_F^0, and V_F^+ can be given by:

$$\begin{cases} V_F^- = V_x \dfrac{Z_{th}^-}{Z_{th}^- + R_{ph}} \\ V_F^0 = V_x \dfrac{Z_{th}^0}{Z_{th}^0 + R_{ph} + 3R_g} \\ V_F^+ = V_x\left(1 + \dfrac{R_{ph}}{Z_{th}^- + R_{ph}} + \dfrac{R_{ph}}{Z_{th}^0 + R_{ph} + 3R_g}\right) \end{cases} \tag{A3}$$

Accordingly, V_F^-/V_F^0 and V_F^-/V_F^+ are determined by:

$$\begin{cases} \dfrac{V_F^-}{V_F^0} = \dfrac{Z_{th}^-}{Z_{th}^0} \dfrac{Z_{th}^0 + R_{ph} + 3R_g}{Z_{th}^- + R_{ph}} \\ \dfrac{V_F^-}{V_F^+} = \dfrac{Z_{th}^-}{Z_{th}^- + 2R_{ph} + \dfrac{R_{ph}\left(R_{ph} + Z_{th}^-\right)}{Z_{th}^0 + R_{ph} + 3R_g}} \end{cases} \tag{A4}$$

APPENDIX B

The maximum magnitude of each phase current, i.e., $I_{peak_{a,b,c}}$, can be represented in terms of PS and NS currents as:

$$I_{peak_{a,b,c}} = \left(\left| I_{IBR}^{+} \right|^2 + \left| I_{IBR}^{-} \right|^2 + 2 \left| I_{IBR}^{+} \right| \left| I_{IBR}^{-} \right| \cos\left(\varphi_{a,b,c} + \angle I_{IBR}^{+} - \angle I_{IBR}^{-} \right) \right)^{\frac{1}{2}} \quad \text{(B1)}$$

where $\varphi_{a,b,c}$ represents phase shift 0°, −120°, and 120° for phases *a*, *b*, and *c*, respectively. To avoid any phase current from exceeding its maximum limit, the limit current I_{limit} is equivalent to the maximum phase, which is calculated by:

$$I_{peak} = \left(\left| I_{IBR}^{+} \right|^2 + \left| I_{IBR}^{-} \right|^2 + 2 \left| I_{IBR}^{+} \right| \left| I_{IBR}^{-} \right| \max\left\{ \cos\left(\varphi_{a,b,c} + \angle I_{IBR}^{+} - \angle I_{IBR}^{-} \right) \right\} \right)^{\frac{1}{2}} \quad \text{(B2)}$$

According to (B2), the maximum value of $\left| I_{IBR}^{+} \right|$ is determined when the value of $\max\left\{ \cos\left(\varphi_{a,b,c} + \angle I_{IBR}^{+} - \angle I_{IBR}^{-} \right) \right\}$ is the minimum, which is equal to 0.5 when $\angle I_{IBR}^{+} - \angle I_{IBR}^{-} = 60°$, 180°, or 300°. Thus, the maximum value of $\left| I_{IBR}^{+} \right|$ is derived from:

$$I_{peak} = \sqrt{\left| I_{IBR}^{+} \right|^2 + \left| I_{IBR}^{-} \right|^2 + \left| I_{IBR}^{+} \right| \left| I_{IBR}^{-} \right|} = I_{limit} \quad \text{(B3)}$$

By substituting (17) into (B3), $\left| I_{IBR}^{+} \right|$ is obtained by:

$$\left| I_{IBR}^{+} \right| = I_{limit} \frac{\left| V_R^{+} \right|^2}{\sqrt{\left| V_R^{+} \right|^2 + \left| V_R^{-} \right|^2 + \left| V_R^{+} \right| \left| V_R^{-} \right|}} \quad \text{(B4)}$$

By substituting (B4) into (22) and keeping $I_{limit} = 1.5$ p. u., $\Delta\theta_{RF}^{\pm}$ can be calculated by:

$$\Delta\theta_{RF}^{\pm} = \sin^{-1}\left(\frac{1.5 \left| Z_R^{\pm} \right|}{\sqrt{\left| V_R^{+} \right|^2 + \left| V_R^{-} \right|^2 + \left| V_R^{+} \right| \left| V_R^{-} \right|}} \sin\left(-\phi^{\pm} + \theta_Z^{\pm} \right) \right) \quad \text{(B5)}$$

REFERENCES

[1] F. Blaabjerg, Y. Yang, D. Yang *et al.*, "Distributed power-generation systems and protection," *Proceedings of the IEEE*, vol. 105, no. 7, pp. 1311-1331, Jul. 2017.

[2] Y. Mohammadi and R. C. Leborgne, "Improved DR and CBM methods for finding relative location of voltage sag source at the PCC of distributed energy resources," *Electrical Power and Energy Systems*, vol. 117, p. 105664, May 2020.

[3] N. George, O. Naidu, and A. Pradhan, "Distance protection for lines connecting converter interfaced renewable power plants: adaptive to grid-end structural changes," *IEEE Transactions on Power Delivery*, vol. 38, no. 3, pp. 2011-2021, Jun. 2023.

[4] Y. Mohammadi and R. C. Leborgne, "A new approach for voltage sag source relative location in active distribution systems with the presence of inverter-based distributed generations," *Electric Power Systems Research*, vol. 182, p. 106222, May 2020.

[5] M. Salehi and F. Namdari, "Fault classification and faulted phase selection for transmission line using morphological edge detection filter," *IET Generation, Transmission & Distribution*, vol. 12, no. 7, pp. 1595-1605, Apr. 2018.

[6] J. Fang, K. Chen, C. Liu *et al.*, "An explainable and robust method for fault classification and location on transmission lines," *IEEE Transactions on Industrial Informatics*, vol. 19, no. 10, pp. 10182-10191, Oct. 2023.

[7] W. Yuan, Y. Li, L. Xu *et al.*, "A fast faulty phase selection method considering fault tolerance for single phase to ground fault in distribution networks," *IEEE Transactions on Instrumentation and Measurement*, vol. 72, pp. 1-12, Sept. 2023.

[8] P. Barman, N. Subhrahmanyam, S. Roy *et al.*, "A statistical feature-based transmission fault identification and classification," in *Proceedings of 2022 IEEE 2nd International Conference on Sustainable Energy and Future Electric Transportation (SeFeT)*, Hyderabad, India, Aug. 2022, pp. 1-6.

[9] *Technical Manual: MiCOMho P446 – Fast Multifunction Distance Protection Pelay*, Alstom, Stafford, U.K., 2011.

[10] *Power Converter with Ground Fault Detection Function and Fault Detection Method*, U.S. Patent no. 11502507, Nov. 2022.

[11] J. Zhang, B. Zhang, and C. Wang, "Improved schemes for traditional current-based phase selectors in wind power systems," *IET Generation, Transmission & Distribution*, vol. 12, no. 21, pp. 5781-5788, Oct. 2018.

[12] G. Song, C. Wang, T. Wang *et al.*, "A phase selection method for wind power integration system using phase voltage waveform correlation," *IEEE Transactions on Power Delivery*, vol. 32, no. 2, pp. 740-748, Apr. 2017.

[13] M. A. Azzouz, A. Hooshyar, and E. El-Saadany, "Resilience enhancement of microgrids with inverter-interfaced DGs by enabling faulty phase selection," *IEEE Transactions on Smart Grid*, vol. 9, no. 6, pp. 6578-6589, Nov. 2018.

[14] M. A. Azzouz and A. Hooshyar, "Dual current control of inverter-interfaced renewable energy sources for precise phase selection," *IEEE Transactions on Smart Grid*, vol. 10, no. 5, pp. 5092-5102, Sept. 2019.

[15] W. Medhat and M. A. Azzouz, "Triple current control of four-wire inverter-interfaced DGs for correct fault type identification," *IEEE Transactions on Smart Grid*, vol. 13, no. 5, pp. 3607-3618, Sept. 2022.

[16] A. A. Aboelnaga, M. A. Azzouz, H. Sindi *et al.*, "Fault ride through of inverter-interfaced renewable energy sources for enhanced resiliency and grid code compliance," *IEEE Transactions on Sustainable Energy,* vol. 13, no. 4, pp. 2275-2290, Oct. 2022.

[17] E. Carrasco, M. Moreno, M. Martínez *et al.*, "Improved faulted phase selection algorithm for distance protection under high penetration of renewable energies," *Energies*, vol. 13, no. 3, p. 558, Jan. 2020.

[18] A. Hooshyar, E. F. El-Saadany, and M. Sanaye-Pasand, "Fault type classification in microgrids including photovoltaic DGs," *IEEE Transactions on Smart Grid*, vol. 7, no. 5, pp. 2218-2229, Sept. 2016.

[19] K. Xu, Z. Zhang, Q. Lai *et al.*, "Fault phase selection method applied to tie line of renewable energy power stations," *IET Generation, Transmission & Distribution*, vol. 14, no. 13, pp. 2549-2557, Jul. 2020.

[20] P. Praveen and V. Kumar, "Faulty phase selection method for microgrid with inverter-interfaced DGs," in *Proceedings of 2023 IEEE IAS Global Conference on Renewable Energy and Hydrogen Technologies (GlobConHT)*, Male City, Maldives, Mar. 2023, pp. 1-5.

[21] S. Paladhi and A. K. Pradhan, "Adaptive fault type classification for transmission network connecting converter-interfaced renewable plants," *IEEE Systems Journal*, vol. 15, no. 3, pp. 4025-4036, Sept. 2021.

[22] A. A. Aboelnaga and M. A. Azzouz, "Adaptive current-angle-based phase selection for microgrids with inverter-interfaced renewable energy sources," *IEEE Transactions on Smart Grid*, vol. 13, no. 1, pp. 417-428, Jan. 2022.

[23] Y. Xie, Y. Liu, Y. Nie *et al.*, "Improved fault phase selection scheme for lines terminated by inverter based resources," in *Proceedings of IEEE PES General Meeting*, Orlando, USA, Jul. 2023, pp. 1-6.

[24] G. Ziegler, *Numerical Distance Protection: Principles and Applications*, 4th ed., Erlangen: Publicis, 2011.

[25] T. Gonen, *Modern Power System Analysis*, 2nd ed., Boca Raton: CRC Press, 2013.

[26] J. Glover, M. Sarma, and T. Overbye, *Power System Analysis and Design*, 5th ed., Stanford: GENAGE Learning, 2012.

[27] P. M. Anderson, *Power System Protection*. New York: IEEE Press, 1998.

[28] Y. Fang, K. Jia, Z. Yang *et al.*, "Impact of inverter-interfaced renewable energy generators on distance protection and an improved scheme," *IEEE Transactions on Industrial Electronics*, vol. 66, no. 9, pp. 7078-7088, Sept. 2019.

[29] *Technical Requirements for the Connection and Operation of Customer Installations to the Medium Voltage Network (TAR Medium Voltage)*, VDE_AR_N_4110, 2018.

Abdallah A. Aboelnaga received the B. Sc. and M. Sc. degrees (Hons.) in electrical power engineering from Ain Shams University, Cairo, Egypt, in 2014 and 2018, respectively, and the Ph.D. degree in electrical and computer engineering from the University of Windsor, Windsor, Canada, in 2023. He is currently on leave with the Department of Electrical Power and Ma-

chines Engineering, Ain Shams University. He is currently a Postdoctoral Fellow with the Power and Energy System Research Group, University of Windsor. His research interests include protection of smart grid, control of power electronic converters, and control of renewable energy sources.

Maher A. Azzouz received the B.Sc. and M.Sc. degrees (Hons.) in electrical power engineering from Cairo University, Cairo, Egypt, in 2008 and 2011, respectively, and the Ph.D. degree in electrical and computer engineering from the University of Waterloo, Waterloo, Canada, in 2016. He was a Postdoctoral Fellow with the Power and Energy System Group, University of Waterloo. He is currently on leave with the Department of Electrical and Computer Engineering, University of Windsor, Windsor, Canada, and is with the Electrical Engineering Department, Qatar University, Doha, Qatar. His research interests include control of power electronic converters, power system protection, distribution system operation and planning, and renewable energy sources.